Low Temperature Physics/Fizika Nizkikh Temperatur, 2014, v. 40, No. 4, pp. 389–399

Electronic structure, Fermi surface and dHvA effect in YIn_3, $LuIn_3$, and $YbIn_3$

V.N. Antonov

Institute of Metal Physics, 36 Vernadsky Street, 03680 Kiev-142, Ukraine
E-mail: antonov@imp.kiev.ua

Received June 26, 2013

The electronic structure, Fermi surface, angle dependence of the cyclotron masses and extremal cross sections of the Fermi surface of RIn_3 (R = Y, Lu, and Yb) compounds were investigated from first principles using the fully relativistic Dirac linear muffin-tin orbital method. The effect of the spin-orbit (SO) interaction and Coulomb repulsion U in a frame of the LDA+SO+U method on the Fermi surface, orbital dependence of the cyclotron masses, and extremal cross sections of the Fermi surface are examined in details. A good agreement with experimental data of cyclotron masses and extremal cross sections of the Fermi surface was achieved.

PACS: 75.50.Cc Other ferromagnetic metals and alloys;
71.20.Lp Intermetallic compounds;
71.15.Rf Relativistic effects.

Keywords: Fermi surface, band structure, rare earth compounds.

1. Introduction

The de Haas–van Alphen (dHvA) effect is an oscillatory variation of the diamagnetic susceptibility as a function of a magnetic field strength (B). The method provides details of the extremal areas of a Fermi surface (FS). The first experimental observation of this behavior was made by Wander Johannes de Haas and his student P.M. van Alphen in 1930 [1]. They have measured a magnetization M of semimetal bismuth as a function of the magnetic field and found that the magnetic susceptibility M/B is a periodic function of the reciprocal of the magnetic field ($1/B$). Similar oscillatory behavior has been also observed in magnetoresistance (so-called the Shubnikov–de Haas effect). The dHvA phenomenon was explained by Landau [2] as a consequence of the quantization of closed electronic orbits in a magnetic field. The electrons in a metal exist only as a series of orbitally quantized states in a magnetic field. Because the number of occupied Landau levels changes with the magnetic field, on sweeping the magnetic field one observes oscillations in the magnetization which are periodic in an inverse magnetic field.

Although the magnetic oscillations were discovered as long as 1930 in bismuth, it was nearly 20 years before the effect was found in other metals [3]. Bismuth contains very few conduction electrons and so has a very small Fermi surface. The significance of a small Fermi surface is that the oscillations being of low frequency and requiring only modest magnetic field are particularly easy to observe. Higher fields and more sensitive techniques are necessary for seeing the oscillations in most other metals and it was mainly for this reason that the effect was not more widely observed until the late 1940s, while the very high frequency oscillations associated with the large Fermi surfaces of monovalent noble and alkali metals were observed only in the late 1950s [4].

The connection between the oscillations and the Fermi surface was pointed out independently by I.M. Lifshitz (1950) and by Onsager (1951), fortunately at just the time when the oscillations were being discovered in more and more metals. For majority of the metals the oscillation proved to be much more complicated than those in bismuth. It was Lifshitz–Onsager formulation that provided the key to unraveling the rather complicated experimental data.

Onsager during his visit Cambridge in 1951 pointed out that the change in $1/B$ through a single period of oscillation was determined by the remarkably simple relation

$$P = \frac{1}{F} = \Delta\left(\frac{1}{B}\right) = \frac{2\pi e}{\hbar c S_F}, \qquad (1)$$

where P is the period of the dHvA oscillation in $1/B$, F is the dHvA frequency, and S_F is any extremal cross-sectional area of the Fermi surface in a plane normal to the magnetic field. Later Onsager published his idea in Ref. 5. Similar idea has been proposed by I.M. Lifshitz in an unpublished lecture in Academy of Sciences of Ukraine in 1950. Later on I.M. Lifshitz and A.M. Kosevich derived

a rigorous general form of the oscillatory magnetization which gives not only the oscillation frequency but also their amplitude and phase [6,7].

If the z axis is taken along the magnetic field, then the area of a Fermi-surface cross section at height k_z is $S(k_z)$ and the extremal areas S_F are the values of $S(k_z)$ at the k_z where $S(k_z)/k_z = 0$. Thus maximum and minimum cross sections are among the extremal ones. Since altering the magnetic field direction brings different extremal areas into play, all extremal areas of the Fermi surface can be mapped out. From the temperature and field dependences of the dHvA amplitude, the cyclotron effective mass m_c^* can be determined. The mean free path l can be also estimated from the simple relations: $S_F = \pi k_F^2$, $\hbar k_F = m_c^2 v_F$, and $l = v_F \tau$, where k_F is half of the caliper dimension of a circular S_F and v_F is the Fermi velocity. Although, the dHvA experiment needs high-quality single crystals as well as low temperatures down to 30 mK and strong magnetic fields up to 170 kOe, it provides quite precious information on the Fermi surface of crystals.

De Haas–van Alphen effect is a powerful tool to explore the electronic structure of metals. To prove it we consider two examples in the present study. First, we compare the band structure and Fermi surface of isostructural and isoelectronic compounds YIn_3 and $LuIn_3$. We will show that even a small change of the Fermi-surface properties associated with the relativistic effects can be precisely detected by the dHvA measurements.

The second example is strongly correlated $YbIn_3$ compound with divalent Yb^{2+} ions. For this compound we performed three independent fully relativistic band structure calculations. The 4*f* electrons have been considered as: (1) itinerant electrons using the local density approximation (LDA+SO); (2) fully localized, putting them in the core; and (3) partly localized using the LDA+SO+*U* approximation. We will show that the dHvA method can be suited as ideal method for the decision which approximation is more correct for the description of the electronic structure of lanthanide crystals.

The de Haas–van Alphen oscillations in $LuIn_3$ and $YbIn_3$ were measured by Nojiri *et al.* [8]. They also calculated angular dependence of the dHvA frequency in $YbIn_3$ using 4*f*-localized model in a frame of full potential linear augmented plane wave (FLAPW) method. They found quite good agreement between the theory and the experiment for high-frequency ellipsoidal type α, β, and γ orbits. Although, the agreement with the experiment for the low-frequency δ orbits was worse and the ξ orbits were not described at all. The angular dependencies of the de Haas–van Alphen frequencies and the corresponding cyclotron masses for YIn_3 were determined by Pluzhnikov *et al.* [9]. The dHvA frequency branches were in the range from $2.3 \cdot 10^6$ to $105 \cdot 10^6$ Oe. For all of them cyclotron masses were found to be light; their values were between 0.2 m_0 and 0.8 m_0. Fermi-surface properties in rare earth (R) and actinide (An) compounds of RX_3 (X = Al, Ga, In, Si, Ge, Sn, Pb), AnX_3, $RTIn_5$ (T: transition metal), and $AnTGa_5$ are presented in recent review article by Onuki and Settati [10].

The paper is organized as follows. Section 2 presents the details of the calculations. Section 3 is devoted to the electronic structure as well as the Fermi surface, angle dependence of the cyclotron masses and extremal cross sections of the Fermi surface in RIn_3 (R = Y, Lu, and Yb) using the fully relativistic linear muffin-tin orbital (LMTO) band structure method. The results are compared with available experimental data. Finally, the results are summarized in Sec. 4.

2. Computational details

The RIn_3 (R = Sc, Y, La, Lu, and rare earth elements) compounds crystallize in the $AuCu_3$-type cubic crystal structure with the space group symmetry $Pm\bar{3}m$ (number 221), where the corner-sites are occupied by the R atoms and the face-centered sites are occupied by the In atoms (Fig. 1). Most RIn_3 compounds order antiferromagnetically, except a paramagnet of $PrIn_3$ with the singlet ground state in the CEF scheme. YIn_3 and $LuIn_3$ are Pauli paramagnets [10]. $YbIn_3$ is also a divalent Pauli paramagnet.

Determination of the energy band structure of solids is a many-body problem. Band theory, a mean-field theory to treat this problem, in the framework of the local density approximation, has been successful for many kinds of materials, and has become the *de facto* tool of first-principle calculations in solid state physics. It has contributed significantly to the understanding of material properties at the microscopic level. However, there are some systematic errors which have been observed when using the LDA. In particular, the LDA fails to describe the electronic structure and properties of 4*f*-electron systems in which the interaction among the electrons is strong. They now called strongly correlated electron systems and many new concepts to address these phenomena have been constructed. However, the understanding of these systems is not complete.

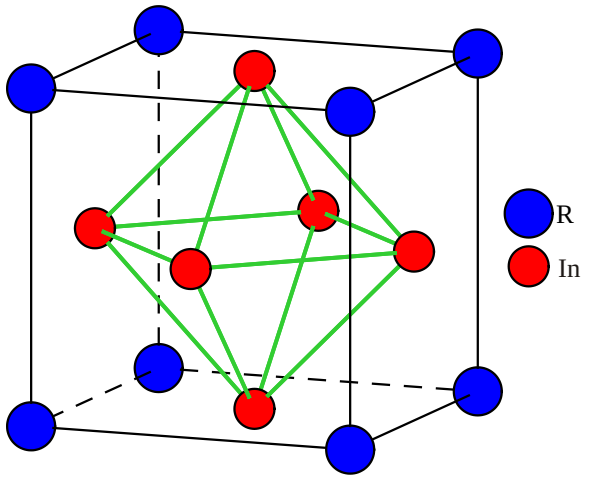

Fig. 1. (Color online) Schematic representation of the RIn_3 crystal structure.

There are actually different attempts to improve the LDA to treat correlated electrons: GW approach, dynamical mean-field theory, time-dependent density functional theory, self-interaction correction, and LDA+*U* method being the most used ones [11,12]. To account better for the on-site *f*-electron correlations, we have adopted as a suitable model the LDA+*U* approach [13,14].

A rigorous formulation for the quasiparticle properties of solids is the Green function approach. The self-energy $\Sigma = G_0^{-1} - G^{-1}$ of the single-particle Green function G is energy dependent and yields the correlation corrections to the single-particle (mean-field) approximation to the quasiparticle excitation spectrum described by G_0. With a number of plausible assumptions, the LDA+*U* approach has been related to the so-called GW approximation to Σ in Ref. 15. Already the simplest random phase approximation applied to Σ for the Hubbard model yields a jump of $\Sigma(\varepsilon)$ at the Fermi level ε_F by the Hubbard *U*. The more elaborate analysis of Ref. 15 results in a correlation correction to the mean-field approximation of the self-energy, which is $U_{\text{eff}}/2$ downward below the Fermi level and $U_{\text{eff}}/2$ upward above the Fermi level. As mean-field theory in a crystal describes always a delocalized situation and the LDA Kohn–Sham potential is a well proved approximation to the self-energy of weakly correlated situations [16], the suggestion is

$$\Sigma(\mathbf{r},\mathbf{r}';\varepsilon) \approx \delta(\mathbf{r}-\mathbf{r}')v_{LDA}(\mathbf{r}) + \\ + P_m \frac{U_{\text{eff}}}{2}[\theta(\varepsilon-\varepsilon_F)-\theta(\varepsilon_F-\varepsilon)]P_m, \qquad (2)$$

where P_m is the projector onto a strongly correlated m state.

The LDA+*U* approach simply uses (2) to replace the LDA Kohn–Sham potential in the self-consistency loop. This can be considered as a rough approximation to Σ. Since the potential shift is taken to be constant in space, it does not deform the Kohn–Sham orbital φ_m. However, it shifts the levels of strongly correlated motion away from the Fermi level and thus removes incorrect hybridization with conduction states, which would spoil the calculated ground-state spin density. On the other hand, being also understood as an approximation to Σ, it hopefully yields for the Kohn–Sham band structure the same quality of a working approximation to the quasiparticle excitation spectrum as it does in the case of weakly correlated metals. Estimates for U_{eff} may be obtained from constrained density functional calculations or from GW calculations in which case the approach is parameter-free. Most reliable are those results which do not very sensitively depend on the actual value of U_{eff} within a certain reasonable range.

The calculations of the electronic structure and Fermi-surface properties of RIn_3 compounds were performed using the fully relativistic spin-polarized Dirac LMTO method [17,18] in the atomic sphere approximation (ASA) with the combined correction term taken into account. We used the von Barth–Hedin parameterization [19] for the exchange-correlation potential. Brillouin zone (BZ) integrations were performed using the improved tetrahedron method [20]. For obtaining the self-consistent solution we used 286 *k* points in the irreducible part of the BZ. For the calculation of the Fermi-surface properties we used extended mash with 22945 *k* points in the irreducible part of the BZ.

We have adopted the LDA+*U* method [13] as a different level of approximation to treat the electron–electron correlations. The LDA+*U* method has proved to be an efficient and reliable tool for calculating the electronic structure of systems where the Coulomb interaction is strong enough to cause localization of the electrons. We used the rotationally invariant LDA+*U* method described in details in our previous paper [14]. The effective on-site Coulomb repulsion *U* was considered as an adjustable parameter and was chosen to 7.0 eV. For the exchange integral *J* the value of 0.82 eV estimated from constrained LDA calculations was used.

3. Results and discussion

3.1. YIn_3 *and* $LuIn_3$

3.1.1. Energy band structure. The Y atom in YIn_3 has no *f* electrons in valence band ($4f^0$ configuration). On the other hand, Lu possesses 14 *f* electrons in valence band ($4f^{14}$ configuration). In our theoretical LDA calculation of the Fermi properties of $LuIn_3$ we treated 4*f* electrons as valence states as well as fully localized ones putting them in core. We found identical FSs for these two approximations. We can conclude that 4*f* states in $LuIn_3$ are strongly localized and have no influence on their Fermi properties. Figure 2 presents the energy band structure and total density of states (DOS) of YIn_3 (full lines) and $LuIn_3$ (dashed lines). The partial DOSs for YIn_3 are shown in Fig. 3. The crystal field at the Y (Lu) site (*Oh* point symmetry) causes the splitting of Y (Lu) *d* orbitals into a doublet e_g (d_{3z^2-1} and $d_{x^2-y^2}$) and triplet t_{2g} (d_{xy}, d_{xz}, and d_{yz}). The crystal field at the In site (*D*4*h* point symmetry) causes the splitting of In *p* orbitals into a singlet a_{2u} (p_x) and a doublet e_u

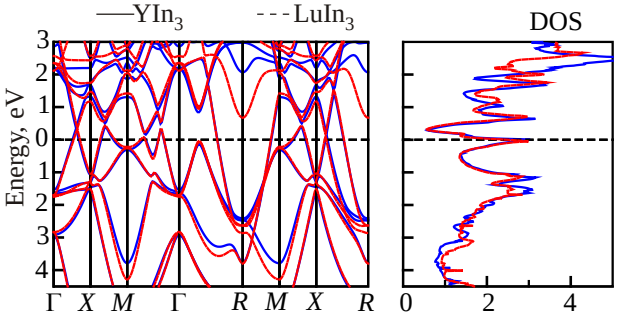

Fig. 2. (Color online) Energy band structure and total DOS [in states/(cell·eV)] of YIn_3 (full blue curves) and $LuIn_3$ (dashed red curves).

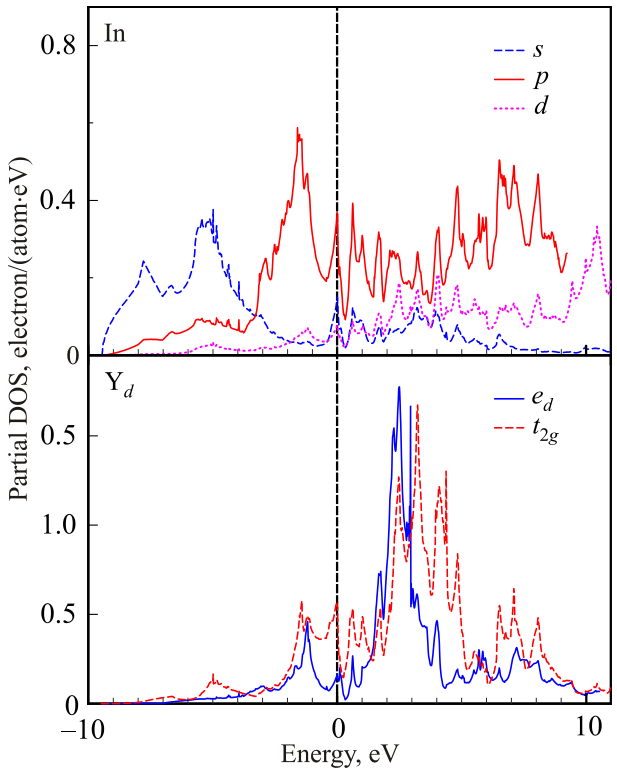

Fig. 3. (Color online) Partial DOSs of YIn_3.

(p_y and p_z). There is a significant In *p*–Y *d* hybridization in the valence band. If one moves from YIn_3 to $LuIn_3$ the *p* valence bandwidth is slightly increasing due to the increasing extension of the corresponding atomic wave functions. The relativistic effects decrease the center of gravity of Lu 6*s* valence bands in comparison with the Y 5*s* bands.

Although, the energy band structures of YIn_3 and $LuIn_3$ compounds are very similar (Fig. 2), there are some significant differences in the band positions. For example, the 8th empty energy band at the R symmetry point shifts downwards by 1.4 eV in $LuIn_3$ in comparison with the YIn_3 due to the relativistic effects. Also the 4th occupied energy band in the M symmetry point is shifted downwards by 0.5 eV in $LuIn_3$. Both these bands are predominantly of *s* character (Lu 6*s* in $LuIn_3$ and Y 5*s* in YIn_3). However, such dramatic change in the position of some energy bands has small influence on the relative positions which cross the ε_F. Two energy bands cross the ε_F in both the compounds: the 6th and 7th energy bands in YIn_3 and the 13th and 14th ones in $LuIn_3$. These bands have predominantly Y (Lu) d (t_{2g}) and In p (e_u) characters. However, there is at least one visible difference in these bands behavior. In the $\Gamma - R$ symmetry direction the 6th energy band lays below ε_F in YIn_3, however, the corresponding 13th band in $LuIn_3$ crosses the ε_F at around 1/3 distance from Γ to R points. As a result, $LuIn_3$ possesses closed electron sheet centered around Γ point in comparison with open one in YIn_3 (see below).

3.1.2. Fermi surface. The electronic configuration of Y atom is $[Kr]\,4f^0 4d^1 5s^2$, while the configuration of Lu atom is $[Xe]\,4f^{14} 5d^1 6s^2$, the valence electrons of In atom are $5s^2 5p^1$. The total number of valence electrons is 12 in YIn_3 and 26 in $LuIn_3$. Therefore, both YIn_3 and $LuIn_3$ are a compensated metals with equal number of electrons and holes, or equal volume of the electron and hole Fermi surfaces. Figure 4 shows the Fermi surface of YIn_3, the corresponding Fermi surface for $LuIn_3$ can be found in Ref. 8 (Fig. 2). The Fermi surfaces of YIn_3 and $LuIn_3$ are very similar and consist of three kinds of major parts. Among them, the nearly spherical electron Fermi surface centered at the corner R points (Fig. 4, lower panel) originated from the 7th energy band in YIn_3 and 14th band in $LuIn_3$; a complex open along the <100> direction hole surface centered at Γ point (Fig. 4, upper panel) from the 6th

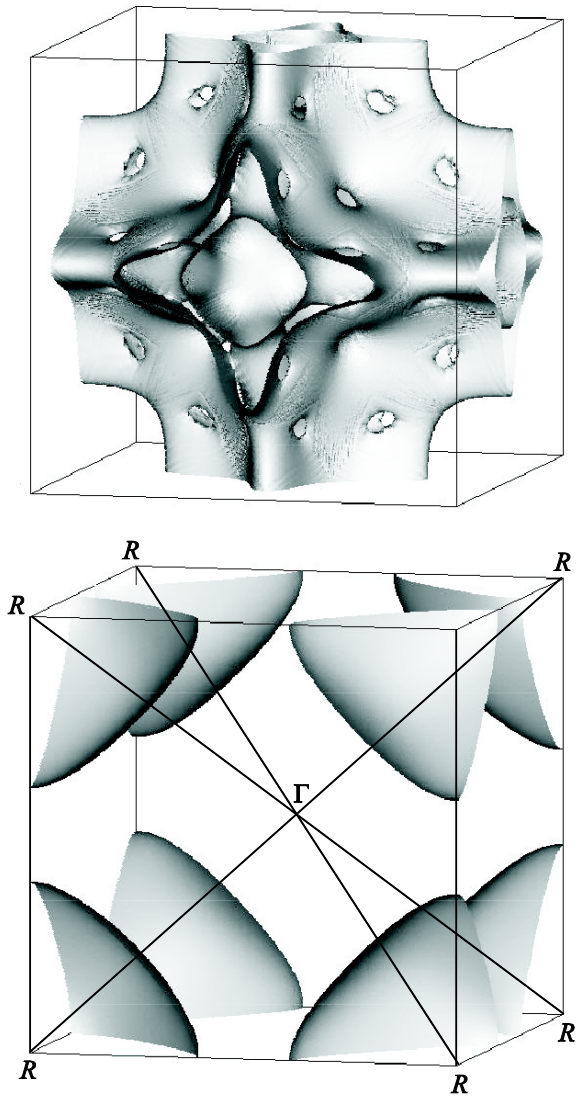

Fig. 4. (Color online) The calculated hole sheets from the 6th energy band (upper panel) and electron sheet of the Fermi surface around R symmetry point from the 7th energy band (lower panel) in YIn_3.

energy band in YIn_3 and 13th band in $LuIn_3$; and almost spherical in topology electron Fermi surface at Γ point. The last sheet of the Fermi surface derived from the 6th energy band in YIn_3 and 13th band in $LuIn_3$ has different topology in these compounds. It is closed in $LuIn_3$ and open in the <111> direction in YIn_3. The difference is clearly seen in Fig. 5 where we present the calculated Fermi-surface cross-section areas of YIn_3 and $LuIn_3$ in the plane perpendicular to the <111> direction at the 1/3 distance between the Γ and *R* points.

Figure 6 presents the calculated Fermi-surface cross-section areas of YIn_3 (left column) and $LuIn_3$ (right column) in the planes perpendicular to the *z* direction and cross *R* symmetry point (upper row), cross Γ point (lower row) and in the planes at 1/3 (the second row from the bottom) and 2/3 (the third row from the bottom) distances between the planes crossed the Γ and *R* points. The cross-sections areas of almost spherical FSs centered in *R* points (red dashed curves) are almost identical in the shape and size for YIn_3 and $LuIn_3$. The cross sections for electron and hole FSs centered in Γ point are also similar in both compounds in the plane $z = 0$ (lower row in Fig. 6). However, for other three planes the cross sections are significantly differ from each other in YIn_3 and $LuIn_3$ not only in size but also in topology. These differences are well reflected in the experimentally measured dHvA frequencies.

Figure 7 shows the angular dependence of the dHvA frequency in YIn_3 and $LuIn_3$ for field directions in the (110) and (1$\bar{1}$0) planes. The black full squares represent the results of dHvA experimental measurements by Pluzhnikov *et al.* [9] in YIn_3 (left panel) and by Nojiri *et al.* [8] in $LuIn_3$ (right panel). Branch α originates from the band 7-electron FS centered in *R* point in YIn_3 (14-electron FS in $LuIn_3$) with the nearly spherical topology, while the others originate from the band 6-hole and 6-electron FSs centered in Γ point. The electron FSs around *R* point have almost identical form and slightly different size in YIn_3 and $LuIn_3$. As a result, they have similar Fermi-surface cross-section areas (α orbits) at all the planes (Fig. 7). The β_1 branch originates from the belly orbit in the band 6-electron FS in YIn_3 (13-electron in $LuIn_3$) centered at the Γ point. As we pointed out above, $LuIn_3$ possesses closed

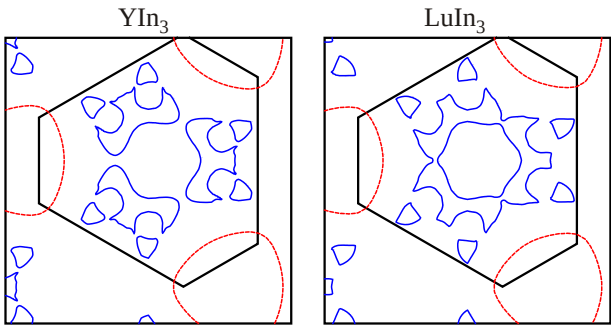

Fig. 5. (Color online) The calculated Fermi-surface cross-section areas of YIn_3 and $LuIn_3$ in the plane perpendicular to the <111> direction at the 1/3 distance between the Γ and *R* points. The full blue curves present the cross sections of surfaces centered in Γ point (for the 6th and 13th energy bands in YIn_3 and $LuIn_3$, respectively); the red dashed curves show the cross sections of electron FSs centered in *R* point (for the 7th and 14th energy bands in YIn_3 and $LuIn_3$, respectively).

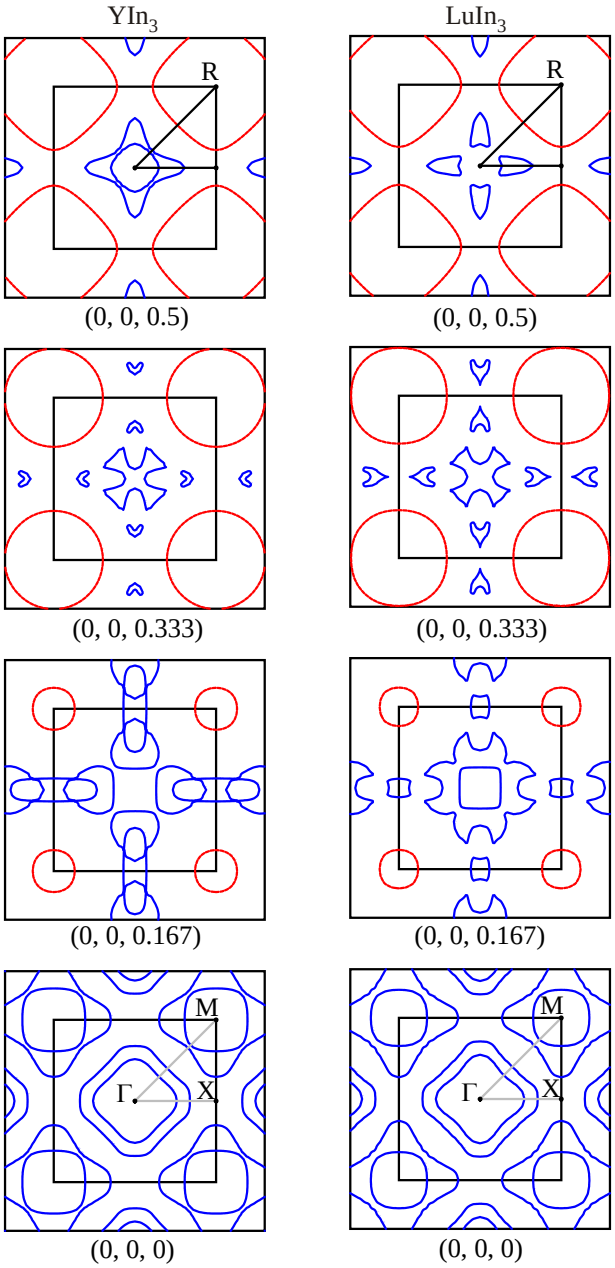

Fig. 6. (Color online) The calculated Fermi-surface cross-section areas of YIn_3 (left column) and $LuIn_3$ (right column) in the planes perpendicular to the *z* direction and cross *R* symmetry point (upper row), cross Γ point (lower row) and in the planes at 1/3 (the second row from the bottom) and 2/3 (the third row from the bottom) distances between the planes crossed the Γ and *R* points. The red dashed curves present electron almost spherical FSs centered in *R* points for the 7th and 14th energy bands in YIn_3 and $LuIn_3$, respectively. The full blue curves present the cross sections of hole and electron surfaces centered in Γ point.

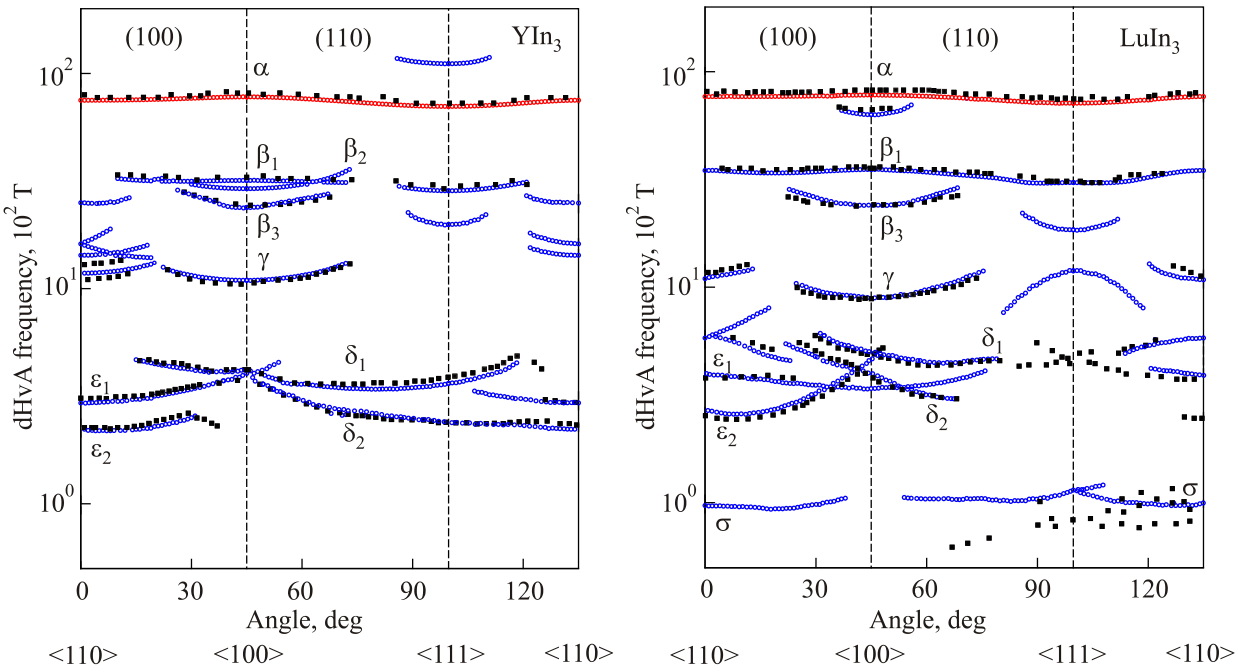

Fig. 7. (Color online) The calculated (open red and blue circles) and experimentally measured (black full squares) in YIn_3 [9] (left panel) and $LuIn_3$ (right panel) [8] angular dependences of the dHvA oscillation frequencies.

electron sheet centered around Γ point in comparison with open one in YIn_3. As a result, the β_1 orbit appears in a whole angle interval in $LuIn_3$ and restricted angle intervals in YIn_3 (±35° around <100> direction and ±15° around <111> direction). The β_3 orbits are also placed on the band 6-electron FS in YIn_3 (13-electron in $LuIn_3$) centered at the Γ point. The γ orbits in both the compounds have similar angular field dependence.

The orbits in the region of the low dHvA frequencies ($F < 0.1$ T) correspond to small sheets of open 6-hole FS in YIn_3 (13-hole in $LuIn_3$) centered at the Γ point. They are sensitive to peculiarities of the electronic structure and have not much similarity between dHvA spectra in YIn_3 and $LuIn_3$. Especially, there is a very small σ orbit in $LuIn_3$ originated from small ellipsoid type FS sheets at the open 13-hole FS cross sections in $LuIn_3$ which is absent in YIn_3.

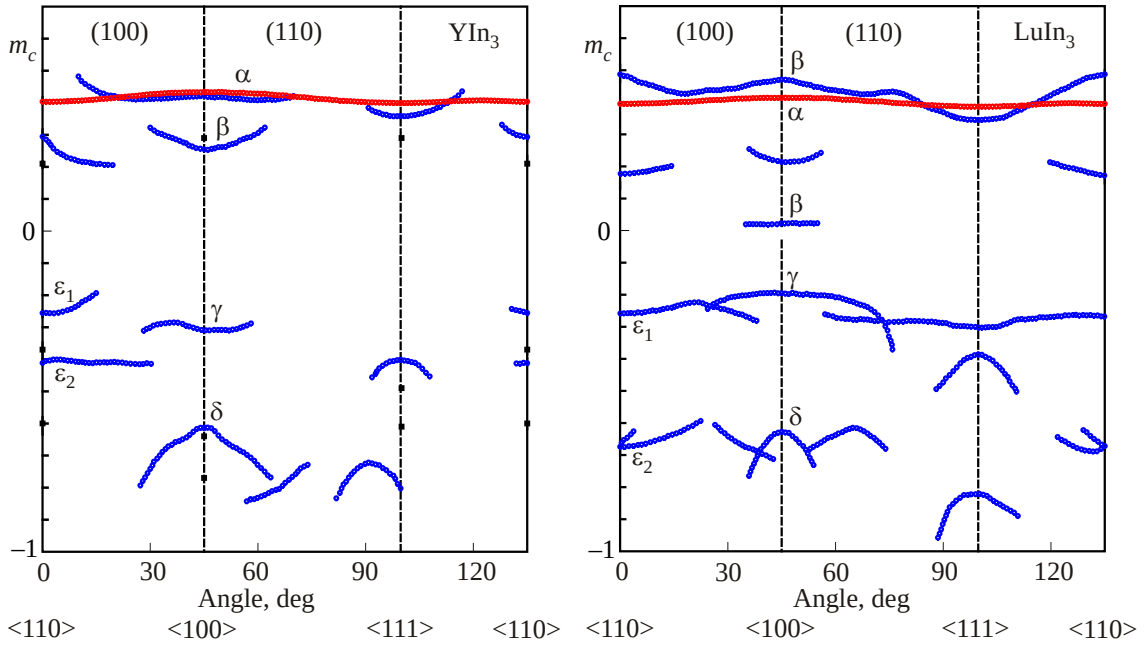

Fig. 8. (Color online) The calculated angular dependence of the cyclotron masses (open red and blue circles) in YIn_3 (left panel) and $LuIn_3$ (right panel) and experimentally measured ones for YIn_3 [9] (black full squares).

The theory reasonably well reproduces the experimentally measured frequencies for the α, β_1, β_3, γ, δ_1, δ_2, ε_1, and ε_2 orbits. However, we were not able to detect low-frequency δ orbits near the <111> direction observed experimentally. Instead, we found an additional two branches with higher frequencies near the <111> direction in $LuIn_3$ which were not detected experimentally. The small σ orbits are detected only at the (110) plane in $LuIn_3$, however, we observed them almost in all angle interval. We also found an additional two branches with higher frequencies near the <111> and <110> directions in YIn_3 which were not detected experimentally.

Figure 8 shows the theoretically calculated angular dependence of the cyclotron masses (m_b) in YIn_3 and $LuIn_3$ and the experimentally measured masses (m_c^*) in YIn_3 in the <110> and <111> and <100> symmetry directions [9]. The cyclotron effective masses were determined from the temperature dependences of the amplitudes of the dHvA oscillations. The cyclotron masses were found to be relatively light in both the compounds. Their values were between –0.9 m_0 and 0.5 m_0. Cyclotron masses for the α orbits have almost constant angle dependence and equal to around 0.4 m_0. We found a stronger angle field dependence for the β_1 orbit in $LuIn_3$ than in YIn_3. The β orbits was found to be strongly anisotropic in both compounds.

We note that band cyclotron effective masses m_b are renormalized by the electron–phonon interaction $m_c^* = m_b(1+\lambda)$, where λ is the constant of the electron–phonon interaction. By comparing the experimentally measured cyclotron masses with band masses we can estimate the λ. It is strongly varied on the orbit type and magnetic direction. We estimate the constant of the electron–phonon interaction to be equal to 0.45 and 0.46 for the ε_1 and ε_2 hole orbits, respectively, with $\mathbf{H}\|$<110>. The constant λ for the electron orbits is equal to 0.48 for the α orbit with magnetic field along <100> direction. For the γ and δ orbits with $\mathbf{H}\|$<100> the λ was found to be equal to 0.8 and 0.34, respectively.

3.2. $YbIn_3$

3.2.1. Electronic structure. The 4*f*-electron lanthanide compounds are usually treated by a 4*f*-localized model (4*f* electrons in core). The localized 4*f*-electron picture is a good starting point in description of the electronic structure of lanthanides. On the other hand, there are several interesting phenomena such as metal–insulator transitions, valence fluctuations in the Kondo effect, heavy fermion behavior, superconductivity, and so on. All these effects strongly depend on the hybridization between 4*f* and conduction electrons and cannot be described correctly in the 4*f*-localized model.

$YbIn_3$ is a Pauli paramagnet with the divalent property of Yb^{2+} [21] ($4f^{14}$ configuration). The divalent property of $YbIn_3$ is clear from the lattice constants of RIn_3 [10], where the lattice constant of $YbIn_3$ deviates from the lanthanide contraction [21]. An important issue is the energy position of the occupied $4f^{14}$ states in the electron band structure of $YbIn_3$. It is well known that LDA usually gives a wrong energy position for the 4*f* states in rare-earth compounds. For nonzero 4*f* occupation it places the 4*f* states right at the Fermi level [22,23] in contradiction to various experimental observations. In the case of Gd compounds or divalent Yb^{2+} compounds the LDA places the 4*f* states too close to the Fermi energy [12,24].

Figure 9 shows the fully relativistic energy band structure of $YbIn_3$. In these calculations the 4*f* states have been considered as: (1) itinerant using the local density approximation, (2) fully localized, treating them as core states, and (3) partly localized using the LDA+*U* approximation. On the first glance all three approximations produce similar electronic structure in the close vicinity of ε_F. The differences are in small details. In the LDA approximation fully occupied 4*f* states of Yb^{2+} are situated at –0.3 eV and –1.65 eV below the Fermi level for the $4f_{7/2}$ and $4f_{5/2}$ states, respectively. The corresponding $4f_{7/2,5/2}$ states in the LDA+*U* approach are located around –1.3 and –2.65 eV below Fermi level. Such shifting of the 4*f*-levels affects the Fermi surface because the 4*f* electrons directly contribute to the conduction electrons.

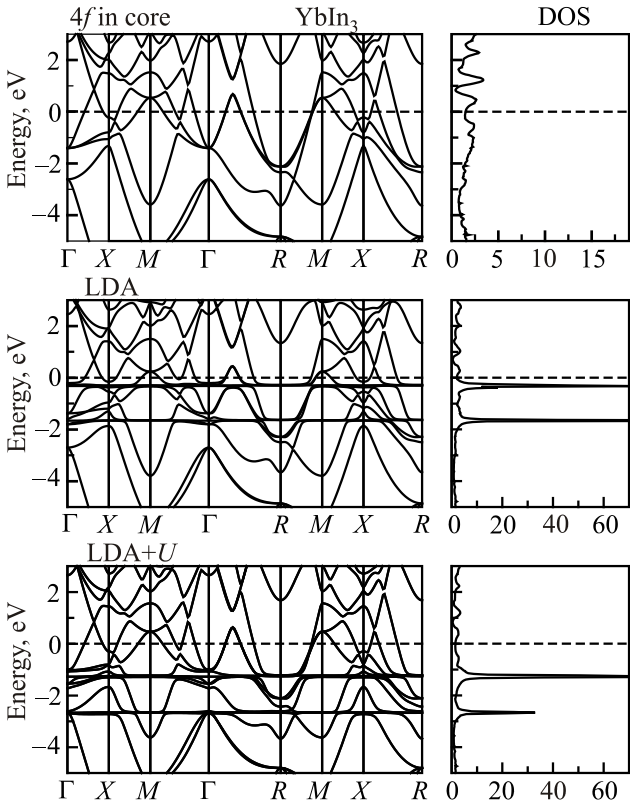

Fig. 9. Self-consistent fully relativistic energy band structure and total DOS (in states/(unit cell·eV)) calculated for $YbIn_3$ treating the 4*f* states as: (1) fully localized with 4*f* in core (upper panel); (2) itinerant LDA approximation (middle panel); and (3) partly localized in the LDA+*U* abroach (lower panel).

3.2.2. Fermi surface. The electronic configuration of Yb atom is [Xe] $4f^{14}6s^2$, the same as in Lu atom but without 5*d* electron. Considering the valence electrons of $5s^25p^1$ in In atom, the total number of valence electrons are 25 (11 in the 4*f*-localized model) in $YbIn_3$, revealing an uncompensated metal. Due to the lack of one electron in valence band the Fermi level of $YbIn_3$ shifts downward in comparison with $LuIn_3$ compound. This leads to significant changing of the Fermi surface coming from $LuIn_3$ to $YbIn_3$. There are three energy bands which cross the ε_F (5th, 6th, and 7th in localized model with 4*f* electrons in core, and 12th, 13th, and 14th bands for the LDA and LDA+*U* approaches).

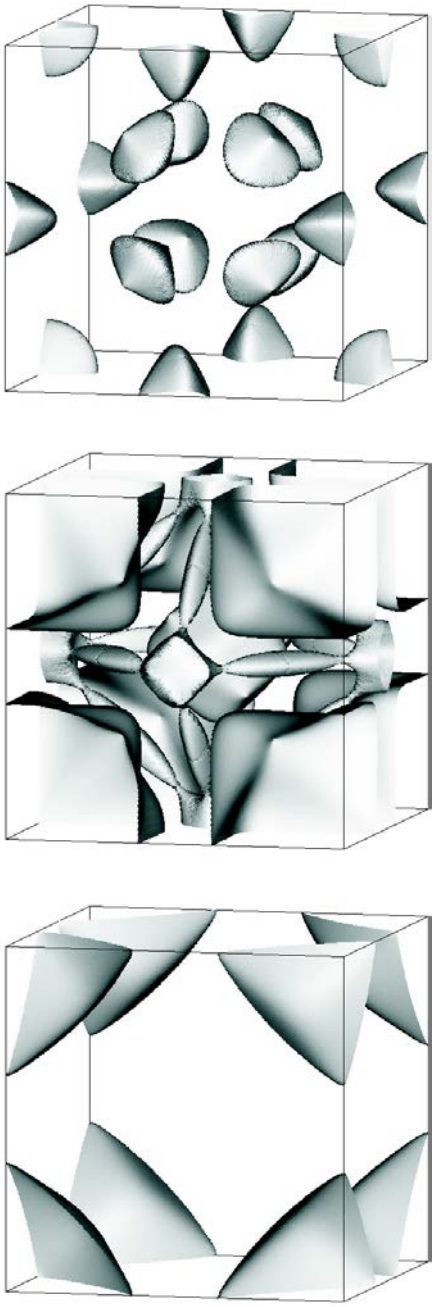

Fig. 10. (Color online) The theoretically calculated band 12-hole (upper panel), 13-hole and electron (middle panel), and band 14-electron (lower panel) Fermi surfaces in $YbIn_3$.

Figure 10 shows the Fermi surface of $YbIn_3$. The 14th energy band (7th in 4*f*-localized model) produces a nearly spherical electron Fermi surface centered at the corner R points (lower panel). This FS is very similar to the corresponding FSs in YIn_3 and $LuIn_3$ (compare lower panels in Figs. 4 and 10). However, already the 13th energy band in $YbIn_3$ produces quite different FS in comparison with YIn_3 and $LuIn_3$ reference compounds. There are several closed sheets derived from the 6th energy band in $YbIn_3$ (middle panel in Fig. 10): electron Fermi surface at Γ point; small electron ellipsoids along $\Gamma - M$ symmetry direction, electron pockets in X point, small hole ellipsoids along $X - R$ direction and a very large electron sheet in R point. Besides, $YbIn_3$ has an additional small closed hole sheets originated from the 12th energy band and situated at M point and along the $\Gamma - R$ direction (upper panel in Fig. 10) which are absent in reference compounds YIn_3 and $LuIn_3$.

Figure 11 shows the calculated Fermi-surface cross-section areas of $YbIn_3$ in the plane perpendicular to the *z* direction and cross Γ symmetry point (left column), cross R point (right column) and in the plane at half distances between the planes crossed the Γ and R points (middle column) with 4*f* electrons in core (upper row),

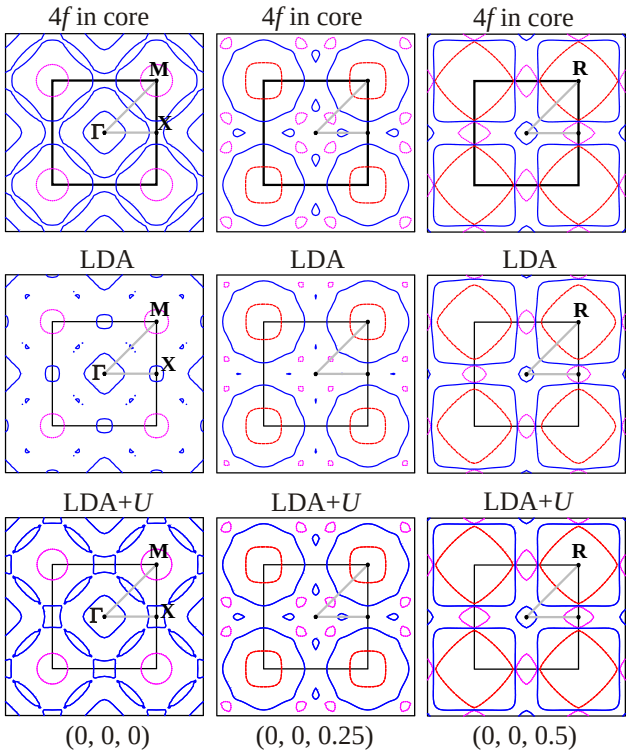

Fig. 11. (Color online) The calculated Fermi-surface cross-section areas of $YbIn_3$ in the plane perpendicular to the *z* direction and cross Γ symmetry point (left column), cross R point (right column) and in the plane at half distances between the planes crossed the Γ and R points (middle column) with 4*f* electrons in core (upper row), LDA (middle row) and LDA+*U* (lower row) approaches. The cross sections of 12-hole sheets present by dotted magenta curves, 13-electron sheets by full blue curves and 14-electron sheets by red dashed curves.

LDA (middle row) and LDA+*U* (lower row) approaches. The cross sections of 12-hole sheets presented by dotted magenta curves, 13-electron and hole sheets by full blue curves and 14-electron sheets by red dashed curves. All three approximations used in the calculations produce similar in topology but different in size cross-sections areas in the planes $2\pi/a$ (0, 0, 0.25) and $2\pi/a$ (0, 0, 0.5). It is interesting to note that cross-section areas obtained with 4*f* electrons in core and LDA+*U* approach are closer to each other than to the LDA calculations. For the plane $z = 0$ all three approximations produce completely different cross-section areas not only in the size but also in topology. A careful comparison of the dHvA results with the results of energy band calculations is therefore necessary to make conclusion which method is more correct for the description of the Fermi-surface properties of $YbIn_3$.

Figure 12 shows the theoretically calculated angular dependence of the dHvA frequency in $YbIn_3$ for field directions in the (100) and (110) planes using the 4*f*-localized model (left panel) and LDA approximation (right panel). The black full squares represent the results of dHvA experimental measurements by Nojiri *et al.* [8]. From the theoretical calculations we found that the branch α originates from the band 14-electron FS centered in R point (7-electron FS with 4*f* in core) with the nearly spherical topology. The β branch originates from the belly orbit in the band 13-electron FS in $YbIn_3$ (6-electron in 4*f*-localized model) centered at the Γ point. The nature of these two orbits is the same as the α and β_1 orbits in YIn_3 and $LuIn_3$. There is an excellent agreement between the experiment and theory with 4*f* electron in core for α orbit, but the LDA approach slightly underestimates the frequencies for this orbit. The fully localized model overestimates and the LDA approach underestimates the frequencies for the β orbit. The π orbit originates from the extremal cross sections of large 13-electron FS centered in R point.

The orbits δ, $\varepsilon_{1,2}$, and $\xi_{1,2}$ in the region of the low dHvA frequencies ($F < 0.1$ T) correspond to small sheets of closed 12-hole FSs situated at M point and along the $\Gamma - R$ direction (upper panel in Fig. 10) as well as to small 13-electron ellipsoids along $\Gamma - M$ symmetry direction, 13-electron pockets in X point, and small 13-hole ellipsoids along $X - R$ direction. They are sensitive to the peculiarities of the electronic structure and have not much similarity with the dHvA experimental data for the 4*f*-localized model as well as for the LDA approach. Especially, 4*f*-localized model strongly overestimates the size of the δ orbits, however, the LDA calculations equally underestimate their size. Both the approaches clearly reproduce the $\varepsilon_{1,2}$ and $\xi_{1,2}$ orbits.

On the other hand, the calculations in the LDA+*U* approach describes the low-frequency orbits quite well (see Fig. 13). This approach also improve the agreement with the experiment for the β orbits. We can conclude that the inclusion of strong Coulomb repulsion in 4*f* shell is very important for the correct description of the Fermi-surface properties of $YbIn_3$.

Figure 14 shows the theoretically calculated angular dependence of the cyclotron masses in $YbIn_3$ using the LDA+*U* approach. The cyclotron masses were found to be relatively light in $YbIn_3$ as it was also in YIn_3 and $LuIn_3$ (compare Figs. 8 and 14). The cyclotron masses in $YbIn_3$ values are between $-0.9\ m_0$ and $0.5\ m_0$. The largest cyclotron masses were obtained for the high-frequency π

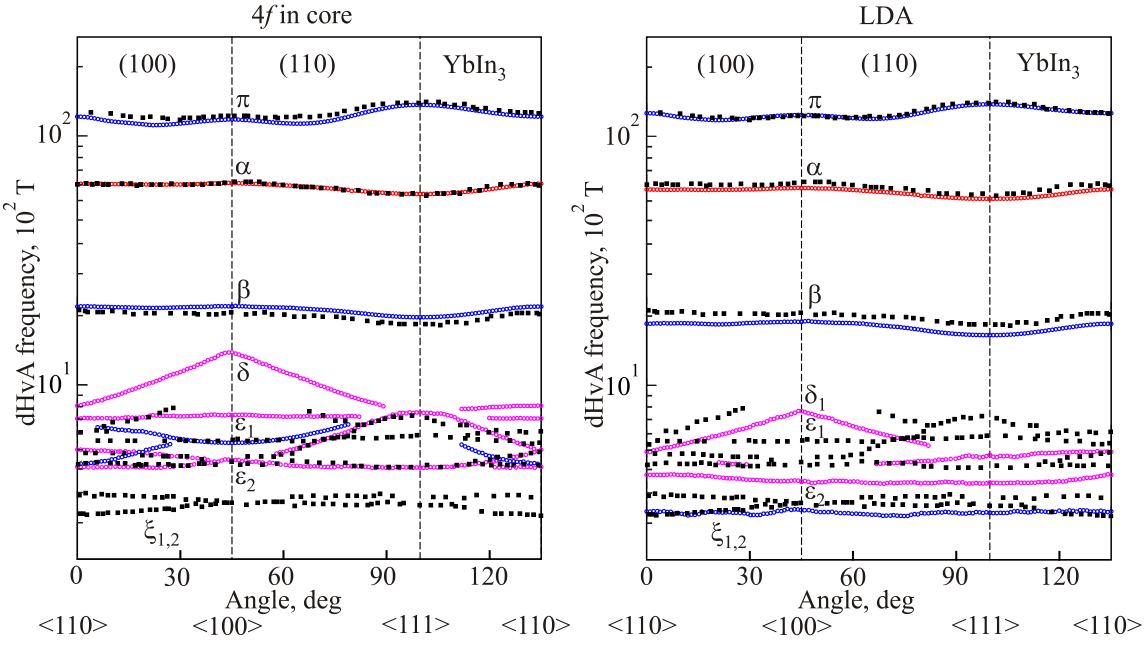

Fig. 12. (Color online) The calculated and experimentally measured [8] (black full squares) angular dependence of the dHvA oscillation frequencies in $YbIn_3$ with 4*f* electrons in core (left panel) and LDA (right panel). The orbits from the 13-hole and electron sheets present by blue circles, 14-electron sheets by red circles and 12-hole sheets by magenta circles.

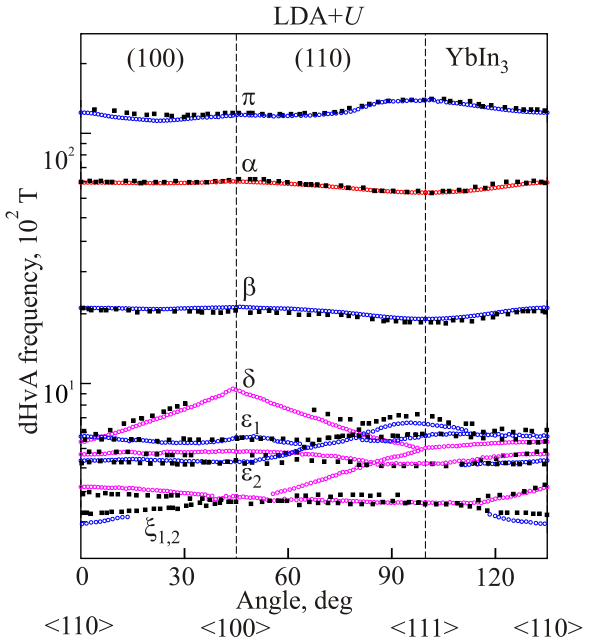

Fig. 13. (Color online) The calculated with the LDA+*U* approach and experimentally measured [8] (black full squares) angular dependence of the dHvA oscillation frequencies in $YbIn_3$. The orbits from the 13-hole and electron sheets present by blue circles, 14-electron sheets by red circles and 12-hole sheets by magenta circles.

electron orbits (0.71–0.78 m_0). Cyclotron masses for the α orbits have almost constant angle dependence and equal to 0.4 m_0. The masses for the π, β as well as the $\xi_{1,2}$ orbits are also have relatively weak angle dependence. The masses for the hole δ orbits were found to be strongly anisotropic in $YbIn_3$.

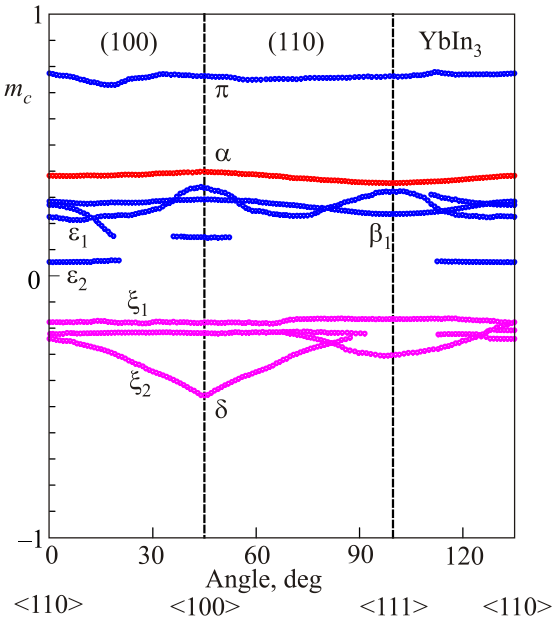

Fig. 14. (Color online) The calculated angular dependence of the cyclotron masses in $YbIn_3$ using the LDA+*U* approach (open blue, red and magenta circles present masses for the 13-hole and electron, 14-electron and 12-hole sheets, respectively).

4. Summary

The electronic structure, the Fermi surface, angle dependence of the cyclotron masses, and extremal cross sections of the Fermi surface of YIn_3, $LuIn_3$, and $YbIn_3$ have been studied using the fully relativistic linear muffin-tin orbital method. The Fermi surfaces of YIn_3 and $LuIn_3$ are very similar and consist of three kinds of major parts: the nearly spherical large electron Fermi surface centered at the corner R points, a complex open along the <100> direction hole surface centered at Γ point, and almost spherical in topology electron Fermi surface at Γ point. The last sheet of the Fermi surface is closed in $LuIn_3$ and open in the <111> direction in YIn_3. The difference in topology and small differences in the size of FS sheets of these two compounds while almost invisible in the band structure picture were clearly detected by the dHvA measurements.

The cyclotron masses were found to be relatively light in both compounds. Their values are between –0.9 m_0 and 0.5 m_0. Cyclotron masses for the α orbits have almost constant angle dependence and equal to around 0.4 m_0. We found a stronger angle field dependence for the β_1 orbit in $LuIn_3$ than in YIn_3. The β orbits were found to be strongly anisotropic in both compounds. The constant of the electron–phonon interaction λ is strongly varied on the orbit type and magnetic direction. We estimate the constant of the electron–phonon interaction in YIn_3 to be equal to 0.45 and 0.46 for the ε_1 and ε_2 hole orbits, respectively, with $\mathbf{H} \parallel$ <110>. The constant λ for the electron orbits is equal to 0.48 for the α orbit with magnetic field along <100> direction. For the γ and δ orbits with $\mathbf{H} \parallel$ <100> the λ was found to be equal to 0.8 and 0.34, respectively.

The second example, considered in this study, is strongly correlated $YbIn_3$ compound with divalent Yb^{2+} ions. For this compound we performed three independent fully relativistic band structure calculations. The 4*f* electrons have been considered as: (1) itinerant electrons using the local density approximation (LDA+SO); (2) fully localized, putting them in the core; and (3) partly localized using the LDA+SO+*U* approximation. The Fermi surface of $YbIn_3$ consists of a nearly spherical 14-electron Fermi surface centered at the corner R points; the 13th energy band produces the electron Fermi surface at Γ point, small electron ellipsoids along $\Gamma - M$ symmetry direction, electron pockets in X point, small hole ellipsoids along $X - R$ direction, and a very large electron sheet in R point; there are also small closed 12-hole sheets situated at M point and along the $\Gamma - R$ direction.

The 4*f*-localized model and the LDA approximation reasonably well reproduces the experimentally measured frequencies for the π, α, and β orbits. The orbits in the region of the low dHvA frequencies (the δ, $\varepsilon_{1,2}$, and $\xi_{1,2}$ orbits) are very sensitive to the peculiarities of the electronic structure. These orbits are clearly reproduced by the 4*f*-localized model as well as by the LDA approach. On the

other hand, the calculations in the LDA+*U* approach quite well describes the low-frequency orbits. The cyclotron masses in $YbIn_3$ were found to be between –0.9 m_0 and 0.5 m_0. The largest cyclotron masses were obtained for the high-frequency π electron orbits (0.71–0.78 m_0). Cyclotron masses for the α orbits have almost constant angle dependence and equal to 0.4 m_0. The masses for the π, β as well as the $\xi_{1,2}$ orbits are also have relatively weak angle dependence. The masses for the hole δ orbits was found to be strongly anisotropic in $YbIn_3$.

In conclusion we found that the Fermi-surface properties of YIn_3 and $LuIn_3$ can be relatively well described by the LDA approach. But the conventional LDA band calculations fails to describe the Fermi surface of $YbIn_3$ due to wrong position of the 4*f* states (too close to the ε_F). The Fermi-surface properties of $YbIn_3$ are also purely described by the 4*f*-localized model because the 4*f* electrons directly contribute to the conduction electrons. On the other hand, the LDA+*U* approach relatively well describes the Fermi surface of $YbIn_3$. We can conclude that the inclusion of strong Coulomb repulsion in 4*f* shell is very important for the correct description of the Fermi-surface properties of $YbIn_3$.

Even nowadays more than 80 year after discovery, de Haas–van Alphen effect is very popular and provides a powerful tool to explore the electronic structure of metals due to its high sensitivity to the peculiarities of the electronic structure. The dHvA method can be regarded as an ideal method for the decision which approximation is more correct for the description of the electronic structure of crystals.

Acknowledgments

This work was supported by the National Academy of Sciences of Ukraine in the framework of the State Target Scientific and Technology Program “Nanotechnology and Nanomaterials” for 2010–2014 (No. 0277092303) and Implementation and Application of Grid Technologies for 2009–2013 (No. 0274092303).

1. W.J. de Haas and P. M. van Alphen, *Proc. Sect. Sci. K. Ned. Akad. Wet*. **33**, 1106 (1930).
2. L. Landau, *Z. Phys*. **64**, 629 (1930).
3. D. Shoenberg, *Magnetic Oscillations in Metals*, Cambridge University Press, Cambridge (1984).
4. D. Shoenberg, *Proc. Roy. Soc. A* **379**, 1 (1982).
5. L. Onsager, *Philos. Mag*. **43**, 1006 (1952).
6. I.M. Lifschitz and A.M. Kosevich, *Dokl. Acad. Scienc. USSR* **96**, 963 (1954).
7. I.M. Lifschitz and A.M. Kosevich, *Zh. Eksp. Teor. Fiz.* **29**, 730 (1955).
8. S. Nojiri, Y. Katayama, D. Aoki, N. Suzuki, K. Sugiyama, R. Settai, Y. Inada, Y. Onuki, and H. Harima, *Physica B* **281**, 747 (2000).
9. V.B. Pluzhnikov, A. Czopnik, and I.V. Svechkarev, *Physica B* **212**, 375 (1995).
10. Y. Onuki and R. Settai, *Fiz. Nizk. Temp*. **38**, 119 (2012) [*Low Temp. Phys*. **38**, 89 (2012)].
11. V.V. Nemoshkalenko and V.N. Antonov, *Computational Methods in Solid State Physics*, Gordon and Breach, Amsterdam (1998).
12. V. Antonov, B. Harmon, and A. Yaresko, *Electronic Structure and Magneto-Optical Properties of Solids*, Kluwer, Dordrecht (2004).
13. V.I. Anisimov, J. Zaanen, and O.K. Andersen, *Phys. Rev. B* **44**, 943 (1991).
14. A.N. Yaresko, V.N. Antonov, and P. Fulde, *Phys. Rev. B* **67**, 155103 (2003).
15. V.I. Anisimov, F. Aryasetiawan, and A.I. Lichtenstein, *J. Phys.: Condens. Matter* **9**, 767 (1997).
16. L. Hedin and B.I. Lundqvist, *J. Phys. C* **4**, 2064 (1971).
17. O.K. Andersen, *Phys. Rev. B* **12**, 3060 (1975).
18. V.V. Nemoshkalenko, A.E. Krasovskii, V.N. Antonov, V.N. Antonov, U. Fleck, H. Wonn, and P. Ziesche, *Phys. Status Solidi B* **120**, 283 (1983).
19. U. von Barth and L. Hedin, *J. Phys. C* **5**, 1629 (1972).
20. P.E. Blöchl, O. Jepsen, and O.K. Andersen, *Phys. Rev. B* **49**, 16223 (1994).
21. I. Harris and G. Raynor, *J. Less-Common Met*. **9**, 7 (1965).
22. V.N. Antonov, B.N. Harmon, and A.N. Yaresko, *Phys. Rev. B* **63**, 205112 (2001).
23. V.N. Antonov, B.N. Harmon, and A.N. Yaresko, *Phys. Rev. B* **66**, 165208 (2002).
24. V.N. Antonov, B.N. Harmon, A.N. Yaresko, and A.P. Shpak, *Phys. Rev. B* **76**, 184422 (2007).